Extraction of Gamow-Teller strength distributions from ^{56}Ni and ^{55}Co via the (p,n) reaction in inverse kinematics

M. Sasano, G. Perdikakis, R. G. T. Zegers, Sam M. Austin, D. Bazin, B. A. Brown, C. Caesar, A. L. Cole, J. M. Deaven, N. Ferrante, C. J. Guess, G. W. Hitt, M. Honma, R. Meharchand, F. Montes, J. Palardy, A. Prinke, L. A. Riley, H. Sakai, M. Scott, A. Stolz, T. Suzuki, L. Valdez, and K. Yako

Phys. Rev. C **86**, 034324 — Published 17 September 2012

DOI: 10.1103/PhysRevC.86.034324

Extraction of Gamow-Teller strength distributions from ^{56}Ni and ^{55}Co via the (p,n) reaction in inverse kinematics

M. Sasano,[1,2,*] G. Perdikakis,[1,2,†] R.G.T. Zegers,[1,2,3,‡] Sam M. Austin,[1,2] D. Bazin,[1] B. A. Brown,[1,2,3] C. Caesar,[4] A. L. Cole,[5] J.M. Deaven,[1,2,3] N. Ferrante,[6] C.J. Guess,[7,2] G. W. Hitt,[8] M. Honma,[9] R. Meharchand,[1,2,3,§] F. Montes,[1,2] J. Palardy,[6] A. Prinke,[1,2,3] L. A. Riley,[6] H. Sakai,[10] M. Scott,[1,2,3] A. Stolz,[1] T. Suzuki,[11,12,13] L. Valdez,[1,2,3] and K. Yako[14]

[1]*National Superconducting Cyclotron Laboratory, Michigan State University, East Lansing, MI 48824-1321, USA*
[2]*Joint Institute for Nuclear Astrophysics, Michigan State University, East Lansing, MI 48824, USA*
[3]*Department of Physics and Astronomy, Michigan State University, East Lansing, MI 48824, USA*
[4]*GSI Darmstadt, Helmholtz-Zentrum für Schwerionenforschung, D-64291, Darmstadt, Germany*
[5]*Physics Department, Kalamazoo College, Kalamazoo, MI 49006, USA*
[6]*Department of Physics and Astronomy, Ursinus College, Collegeville, Pennsylvania 19426, USA*
[7]*Department of Physics, University of Massachusetts Lowell, Lowell, MA 01854, USA*
[8]*Khalifa University of Science, Technology & Research, 127788 Abu Dhabi, UAE*
[9]*Center for Mathematical Sciences, University of Aizu, Aizu-Wakamatsu, Fukushima 965-8580, Japan*
[10]*RIKEN Nishina Center, Wako, 351-0198, Japan*
[11]*Department of Physics, College of Humanities and Sciences, Nihon University, Sakurajosui 3-25-40, Setagaya-ku, Tokyo 156-8550, Japan*
[12]*Center for Nuclear Study, University of Tokyo, Hirosawa, Wako-shi, Saitama 351-0198, Japan*
[13]*National Astronomical Observatory of Japan, Mitaka, Tokyo 181-8588, Japan*
[14]*Department of Physics, University of Tokyo, Tokyo, 113-0033, Japan*

Background: Gamow-Teller (GT) transition strength distributions in stable and unstable pf-shell isotopes are key inputs for estimating electron-capture rates important for stellar evolution. Charge-exchange experiments at intermediate beam energies have long been used to test theoretical predictions for GT strengths, but previous experiments were largely restricted to stable nuclei. Since a large fraction of the nuclei relevant for astrophysical applications (including key nuclei such as ^{56}Ni) are unstable, new methods are needed to perform charge-exchange experiments in inverse kinematics with unstable isotopes.

Purpose: The ^{56}Ni(p,n) and ^{55}Co(p,n) reactions were measured in inverse kinematics in order to extract GT strengths for transitions to ^{56}Cu and ^{55}Ni, respectively. The extracted strength distributions were compared with shell-model predictions in the pf-shell using the KB3G and GXPF1J interactions. By invoking isospin symmetry, these strength distributions are relevant for electron captures on the ground states of ^{56}Ni and ^{55}Ni to final states in ^{56}Co and ^{55}Co, respectively.

Method: Differential cross sections and excitation energy spectra for the ^{56}Ni(p,n) and ^{55}Co(p,n) reactions were determined by measuring neutrons recoiling from a liquid hydrogen target into the low-energy neutron detector array (LENDA). GT contributions to the spectra were extracted using a multipole decomposition analysis and were converted to strengths by employing the proportionality between GT strength and differential cross section at zero linear momentum transfer.

Results: GT strengths from ^{56}Ni and ^{55}Co were extracted up to excitation energies of 8 and 15 MeV, respectively. Shell-model calculations performed in the pf-shell with the GXPF1J interaction reproduced the experimental GT strength distributions better than calculations with the KB3G interaction.

Conclusions: A new technique for measuring (p,n) charge-exchange reactions on unstable nuclei was successfully developed. It can be used to study the isovector response of unstable nuclei in any mass region and for excitation energies beyond the particle decay threshold. In the first experiment, ^{56}Ni(p,n) and ^{55}Co(p,n) reactions were studied and GT transition strengths were extracted for the purpose of testing shell-model calculations used to estimate electron-capture rates in simulations of late stellar evolution. The calculation using the GXPF1J interaction was found to best reproduce the experimental strength distribution.

PACS numbers: 21.60.Cs, 25.40.Kv, 25.60.Lg, 26.30.Jk

* sasano@ribf.riken.jp; Present address: RIKEN Nishina Center, 2-1 Hirosawa, Wako, Saitama 351-0198, Japan
† Present address: Department of Physics, Central Michigan University, Mt. Pleasant, MI 48859, USA
‡ zegers@nscl.msu.edu
§ Present address: Los Alamos National Laboratory, Los Alamos, NM 87545, USA

I. INTRODUCTION

Charge-exchange (CE) reactions at intermediate beam energies ($E_{beam} \geq 100$ MeV/u) have long been used to investigate isovector (change in isospin $\Delta T = 1$) spin-transfer ($\Delta S = 1$) excitations in stable nuclei [1]. One important goal of such experiments is the study of Gamow-Teller (GT) transitions, which are characterized by angular-momentum transfer $\Delta L = 0$ and mediated by the $\vec{\sigma}\tau_{\pm}$ operator. GT strengths extracted from CE experiments are directly connected with weak matrix elements of allowed β-decay and electron capture (EC). GT strengths from weak-decay studies only provide the small portion of the full distribution located within the energy window restricted by the decay Q-value. CE experiments have, therefore, become the main tool to extract the more complete GT response [1, 2].

The GT strengths from CE reaction studies have provided important experimental information for validating theoretical models that are used to estimate weak reaction rates (β-decay and EC capture). These rates are used in simulations of the late evolution of stars prior to their demise as type Ia (thermonuclear) or type II (core-collapse) supernovae (see e.g. Refs. [3, 4] and references therein). Weak reactions on a large number of medium-heavy nuclei (predominantly in the regions of the pf and sdg shells) play an important role in these astrophysical phenomena. However, because of the high temperatures in these environments, EC and β-decay from excited states can also contribute significantly. Hence, it is impossible to determine all relevant GT strength distributions experimentally. Data from CE experiments are used to test and constrain the theory on a limited set of nuclei. Further complicating the situation is that many of the nuclei that play a role are unstable. However, performing CE experiments on unstable nuclei has proven to be a challenge and successful experiments have so far been restricted to relatively light nuclei and to the extraction of the GT strength at low excitation energies [5–9].

In this work, a new technique for measuring the (p,n) CE reaction at ~ 110 MeV/u in inverse kinematics on unstable isotopes is presented. The method relies on measuring the energy and laboratory scattering angle of the recoiling neutron, from which the excitation energy of the residual nucleus and center-of-mass scattering angle are determined. The residual nucleus, or one of its decay products (if the excitation energy exceeds the threshold for decay by particle emission) is also detected to assist in the unambiguous assignment of the reaction channel. The technique is suitable for experiments with unstable isotopes of any mass, up to high excitation energies. The results for ^{56}Ni(p,n) and ^{55}Co(p,n) reactions are presented here; the first successful studies to implement this technique. The main results for ^{56}Ni have been published in Ref. [10]. Here, we provide details and results of that experiment which were not included in the original paper, and also include the results for ^{55}Co, which were obtained simultaneously.

Both ^{56}Ni and ^{55}Co reside in the astrophysically important iron region. In type II supernovae, they are among the nuclei that dominate the change in electron-to-baryon ratio in the pre-supernova stage and thereby affect the structure of the star prior to the collapse [11–13]. In the Chandrasekhar-mass model for type Ia supernovae, ECs on iron-group nuclei take place in the wake of the thermonuclear flame, which leads to a reduction of the pressure and a retardation of the expansion of the star [14]. In addition, EC reactions also reduce the amount of ^{56}Ni produced and thus the brightness of the explosion. Since type Ia supernovae are thought to produce about half of the iron-group nuclei in the universe, models for the progenitor and the explosion can be constrained [15]. However, such constraints require that accurate weak-reaction rates are used in the simulations [14]. Besides the direct role that ^{55}Co and ^{56}Ni play in the above-mentioned astrophysical processes, the data presented here are of broader impact. In particular, the GT strength distribution extracted from the ^{56}Ni(p,n) data can help to improve the theoretical estimates for weak-reaction rates on a larger number of nuclei in the iron group and thus lead to overall better input for astrophysical simulations that rely on weak reaction rates.

The doubly-magic nature of the N=Z=28 nucleus ^{56}Ni has attracted much attention (see e.g. [16–20]). Since both protons and neutrons occupy the same major (pf) shell, the proton-neutron interaction is relatively strong, thereby softening the $f_{7/2}$ core [19, 21]. Shell-model calculations using interactions from the "KB family" [22, 23], which have been used for the generation of a weak-reaction rate library for astrophysical calculations [24], and the "GXPF1 family" [25–27] both predict that the probability of a closed $(f_{7/2})^{16}$ shell configuration for ^{56}Ni is about 65%. However, the GT strength distributions for ^{56}Ni predicted by these interactions differ significantly from each other [27]; the strength distribution calculated with the KB3G interaction is more localized and resides at lower excitation energies. Consequently, EC rates on ^{56}Ni calculated using the KB3G and GXPF1J interactions differ by as much as 30% [27]. Discrepancies of a similar nature are also observed for nearby stable nuclei [4, 27]. Data on ^{56}Ni provide the best possible guidance for understanding and resolving these ambiguities. The additional data collected on ^{55}Co provide insight for a nearby odd-Z,odd-A nucleus and further constrains the theoretical estimates.

By using the (p,n) CE reaction, GT strengths from ^{56}Ni ($T = 0$) and ^{55}Co ($T = \frac{1}{2}$) were extracted in the $\Delta T_z = -1$ (β^-) direction, populating final states in ^{56}Cu and ^{55}Ni, respectively. Because isospin symmetry breaking effects are small, the extracted GT strengths from ^{56}Ni$\rightarrow^{56}$Cu($T = 1, T_z = -1$) also describe the transitions for the ^{56}Ni$\rightarrow^{56}$Co($T = 1, T_z = +1$) reaction (the $\Delta T_z = +1$ (β^+/EC) direction). Similarly, GT strengths extracted for the ^{55}Co$\rightarrow^{55}$Ni transitions also provide information for GT strengths associated with

transitions from ^{55}Ni to ^{55}Co. The method of extracting GT strengths in the β^+/EC direction from $\Delta T_z = -1$, (p,n) data has been used successfully in the past for stable Ni isotopes [28].

A key feature of CE reactions at intermediate beam energies is the proportionality between the differential cross section at 0°, $\sigma_{\rm GT}(0^\circ)$, and the GT strength (B(GT)) associated with the corresponding transition [29]:

$$\sigma_{\rm GT}(0^\circ) = \hat{\sigma}_{\rm GT} F(q,\omega) B({\rm GT}). \quad (1)$$

Here, $F(q,\omega)$ gives the dependence of $\sigma_{\rm GT}$ on the momentum (q) and energy (ω) transfers, and can be reliably calculated by employing a distorted wave impulse approximation (DWIA). $\hat{\sigma}_{\rm GT}$ is the normalization factor of B(GT) referred to as the "GT unit cross section," which depends on the incident energy and target mass. $\sigma_{\rm GT}$ is conveniently extracted from a transition for which the B(GT) is known from β-decay. $\hat{\sigma}_{\rm GT}$ determined in this manner can be applied to GT transitions for which no β-decay data are available. In this work, $\hat{\sigma}_{\rm GT}$ is derived by comparing the measured $\sigma_{\rm GT}(0^\circ)$ value for the transition from ^{55}Co($\frac{7}{2}^-$,g.s.) to ^{55}Ni($\frac{7}{2}^-$,g.s.) with the B(GT) value known from from β^+ decay of ^{55}Ni (logft=3.6) [30]. B(GT) is defined such that it equals 3 for the β-decay of the free neutron.

In the following, the experimental setup (Sec. II) is described, followed by the analysis and results of the experiment (Sec. III) and a comparison with the above-mentioned shell-model calculations (Sec. IV).

II. EXPERIMENT

A. Beam production and beam-particle identification

A 20-pnA, 160 MeV/u beam of ^{58}Ni from the NSCL Coupled Cyclotron Facility struck a 410-mg/cm^2 thick Be production target at the entrance of the A1900 fragment separator [31]. The produced secondary beam was purified by placing a 237-mg/cm^2 thick aluminum wedge at the intermediate image and a momentum-defining slit at the A1900 focal plane. The resulting cocktail beam of $N = 28$ isotones, with a momentum spread of ±0.25%, had an intensity of $\sim 8\times10^5$ pps. It contained secondary beam particles of ^{56}Ni (66%) at 110 MeV/u, ^{55}Co at 106 MeV/u (32%), and ^{54}Fe at 102 MeV/u (2%). Particles were identified on an event-by-event basis by measuring the beam-particle timing relative to the cyclotron radio frequency (RF) signal (42 ns period) with a 1-cm^2 in-beam diamond detector [32] installed at the entrance of the analysis beam line toward the S800 spectrograph [33].

B. Liquid hydrogen target

The reaction target consisted of a liquid hydrogen cell, with an average thickness of 60 mg/cm^2 and a diameter of 35 mm. The hydrogen, kept at a pressure just above 1 atm and a temperature of about 19 K, was contained by 125-μm-thick Kapton foils. The target was placed 65 cm upstream of the pivot point of the S800 spectrograph. To ensure that the cocktail beam of unstable nuclei hit the center of the target cell and did not hit the target frame, it was tuned to a diameter of about 5 mm as observed with a beam viewer made of ZnS painted on a thin aluminum plate. Once the beam spot was checked at the beginning of the experiment, the beam viewer was removed. For the purpose of subtracting background due to events originated from the Kapton foils, data were also acquired with an empty target cell.

C. Low Energy Neutron Detector Array (LENDA)

The liquid hydrogen target was surrounded by the newly constructed Low Energy Neutron Detector Array (LENDA) [34]. LENDA is comprised of 24 neutron detectors, each of which consists of a plastic scintillator bar with photomultiplier tubes attached at each end. In this experiment, 12 bars were placed to the left and to the right of the beam line. The center of each bar was positioned at the beam height and at a distance of 1 m from the target, i.e. the flight-path length (FPL) for the neutrons was 1 m. Each bar had a vertical height of 300 mm ($\Delta\phi = \pm8.5^\circ$), a depth along the axis through the target of 25 mm (ΔFPL/FPL = ±1.3%), and a width of 45 mm ($\Delta\theta = \pm2.6^\circ$). The shaded areas in Fig. 1 show the coverage of the LENDA bars in the coordinate space of neutron energy (E_n) and laboratory angle ($\theta_{\rm lab}$). Laboratory angles between 20° and 70° were covered. The spatial separation between neighboring bars corresponded to a gap in laboratory angle of 1.7°. The total solid angle coverage by LENDA was 0.32 sr. $\theta_{\rm lab}$ was determined on an event-by-event basis from the location of the bar in which a hit was recorded ((x,z)-plane) and by correcting for a small effect (less than 1°) due to the vertical position (y) along the bar. That correction was made based on the assumption that the hits in the y-direction were distributed uniformly along the height of the bar.

The performance of LENDA was characterized in test measurements using radioactive sources as well as by Monte-Carlo simulation, as described in Ref. [35]. The neutron energy (E_n) was determined by measuring the neutron time of flight (TOF), for which the time reference was taken from the diamond detector signal. The absolute TOF scale was obtained by calibrating with prompt γ-rays whose TOF can be reliably calculated from the light velocity and the flight path length. The resolution in neutron energy was estimated to be ±2%, mainly due to ΔFPL/FPL. Even though intrinsic thresholds for neutron-detection of as low as $E_n = 150$ keV can be achieved with LENDA, the threshold for neutron detection was set to $E_n = 200$ keV (35 keV electron-equivalent in units of light output, and corresponding to a TOF

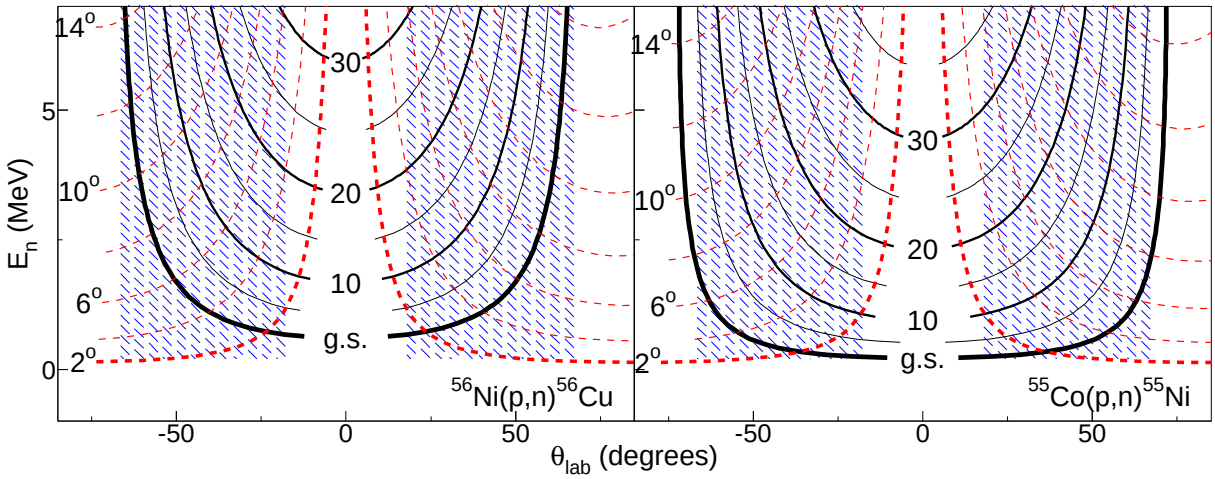

FIG. 1. (Color online) The region (blue shaded area) covered by the LENDA bars in the coordinate space of neutron energy (E_n) and laboratory angle ($\theta_{\rm lab}$). The negative (positive) values of $\theta_{\rm lab}$ correspond to placement of the bars on the left (right) side with respect to the beam line. The continuous curves indicate the correlation between E_n and $\theta_{\rm lab}$ for different values of the excitation energy in the residual nucleus from 0 MeV (g.s.) to 30 MeV with 5-MeV steps. The dotted curves indicate the correlation between E_n and $\theta_{\rm lab}$ for scattering angles in the center-of-mass system ranging from 2° to 12° with 2° steps. The figure on the left (right) is for the ^{56}Ni(p,n) (^{55}Co(p,n)) reaction.

of 160 ns) by software to ensure high precision for the threshold value (which is important for the efficiency estimates) and a uniform treatment of all bars. The measured neutron-detection efficiency for a single bar varied from 40% at $E_n = 0.3$ MeV to 20% at $E_n = 4.0$ MeV. Neutron-detection efficiencies simulated with the Monte-Carlo code MCNP [36] reproduced these efficiencies well [35]. On the basis of that same simulation, the efficiency was estimated to drop off smoothly for neutron-energies in excess of 4 MeV, to 10.7% at $E_n = 10.0$ MeV. It is furthermore noted that in the analysis only events in which a single LENDA bar was hit were used in order to eliminate contributions from cross talk between neighboring bars.

Fig. 2 shows a typical neutron TOF spectrum. Given that the maximum TOF for neutrons originating from scattering events in the target was 160 ns, events with a TOF in excess of that value are due to the background of random coincidences between a neutron event in LENDA and a hit in the diamond detector belonging to different beam bunches. Such random coincidences appear repeatedly (every 42 ns) in the TOF spectra and must be subtracted from the true coincidence signal. This was achieved by duplicating events in the TOF region from 183 to 225 ns (random coincidences only) after shifting in time by multiples of 42 ns. The dashed curve in Fig. 2 shows the TOF spectrum of the simulated events due to random coincidences, which reproduces the repetitive structures observed on top of the smooth neutron spectrum (shown with the continuous curve).

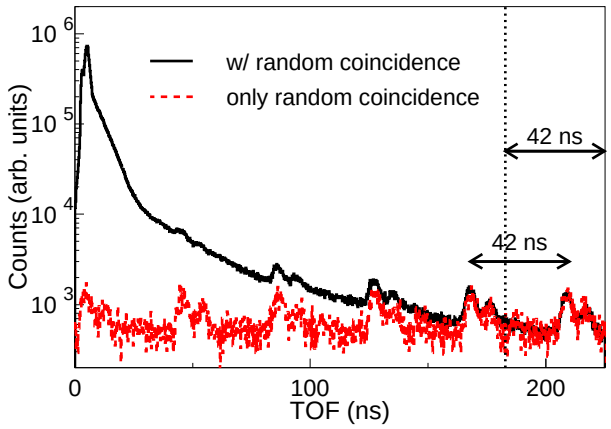

FIG. 2. (Color online) A typical TOF spectrum for the ^{56}Ni(p,n) reaction (continuous curve). A TOF of 150 ns (20 ns) corresponds to a neutron energy of 0.23 MeV (5 MeV). A spectrum due to random coincidence is generated from the data itself by using the events between the vertical dotted line (183 ns) and the right edge of the window (225 ns) and shown with dashed curves. See the text for the details.

D. Particle identification of beam residue

Event-by-event particle identification (PID) for beam residues produced in the target was performed in the S800 spectrograph [33]. The energy loss (ΔE) and TOF of the residues were measured with an ionization chamber and a plastic scintillator, respectively, which were located in the focal plane of the spectrograph [37]. The reference for the TOF measurement was provided by the signal from the in-beam diamond detector. Two cathode-readout drift chambers (CRDC's) provided two-

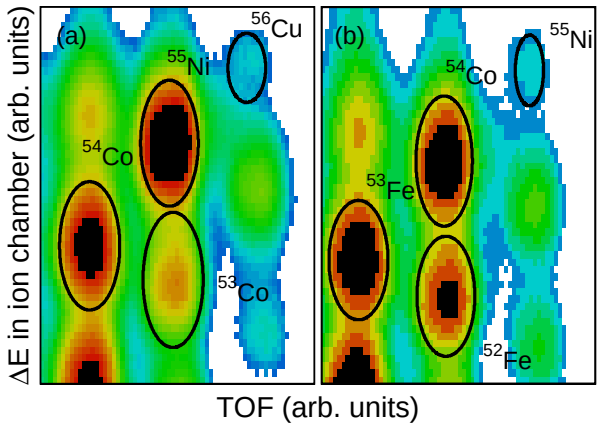

FIG. 3. (Color online) PID spectra in the spectrograph for events associated with the ^{56}Ni component (a) and ^{55}Co component (b) in the beam.

dimensional hit-position information, which was used to determine the momentum and angle of each particle track. The energy-loss and TOF signals were corrected for their dependence on momentum and angle. The PID spectra (energy-loss vs. TOF) for events generated by the ^{56}Ni and ^{55}Co beams are shown in Figs. 3(a) and (b), respectively. PID gates used to select residual particles in the spectrograph are indicated by ovals. Their two-dimensional widths were chosen between 1σ and 2σ to reduce the contamination from neighboring isotopes to very minor levels (see also Sec. III H). The efficiency of PID gates was calculated based on two-dimensional Gaussian distributions in ΔE-TOF space.

Owing to the large angular (20 msr) and momentum ($\pm 3\%$) acceptances of the S800 spectrograph, the trajectories of the beam residues directly produced by the (p,n) reactions as well as heavy fragments associated with their decay by single proton emission were covered in a single setting of the spectrograph's magnetic field. On the other hand, for decay-branches associated with double proton emission (or other multiple-nucleon emissions), the momentum distribution of the residues were too broad to be fully covered in the spectrograph due to the recoil from the decays. Only about 60% of the full momentum distribution was covered in the spectrograph and the absolute magnitudes of the cross sections for these double-proton emission branches could not be reliably calibrated, and thus scaled arbitrarily. This ambiguity can easily be resolved by taking data at several magnetic rigidity settings for the spectrograph, but this was not pursued in the experiment discussed in this paper.

Table I shows the list of selected beam residues and the reaction channels through which the residue was produced. For the ^{56}Ni incoming beam, the ^{56}Cu, ^{55}Ni, ^{54}Co, and ^{53}Co nuclei were selected. The ^{56}Cu nucleus was produced through the ^{56}Ni(p,n)^{56}Cu reaction. Within the excitation-energy region of interest for the extraction of the GT strength distribution, ^{55}Ni and ^{54}Co nuclei could be produced in the decay of ^{56}Cu if the excitation energy exceeded the threshold for decay by single or double proton emission, respectively. However, ^{55}Ni and ^{54}Co nuclei were also produced by knockout/fragmentation reactions of ^{56}Ni on the hydrogen target. These reaction types are associated with the simultaneous emission of fast neutrons at forward scattering angles. These neutrons could scatter indirectly from the surroundings into LENDA and produce false coincidences with events in the S800 focal plane, creating background to the events associated with CE reactions. This background was found to be structureless and largely independent of the nature of the particles detected in the spectrograph. ^{53}Co cannot be the final residue in the decay of ^{56}Cu produced in the CE reaction in the excitation-energy region of interest for the extraction of GT strengths. Therefore, coincidences between ^{53}Co events in the spectrograph and neutron detected in LENDA were used for modeling the background.

Similarly, for the ^{55}Co beam components, ^{55}Ni residues were directly produced in the ^{55}Co(p,n) reaction. In addition, ^{54}Co and ^{53}Fe residues could be produced if the excitation energy in ^{55}Ni exceeded the thresholds for decay by single and double proton emission, respectively. The background due to the knockout/fragmentation reactions was modeled by coincidence events in which ^{52}Fe residues were detected in the S800 focal-plane detectors. The latter fragment cannot be produced in the multi-nucleon decay from ^{55}Ni in the excitation-energy region of interest for the extraction of GT strengths.

III. ANALYSIS AND RESULTS

A. Neutron energy and laboratory scattering angle

Fig. 4 shows scatter plots of E_n versus $\theta_{\rm lab}$ for neutrons detected in LENDA for events associated with the ^{56}Ni beam component. Scatter plots are shown separately for different residue species detected in the spectrograph, as listed in Table I. In Fig. 4(a), a clear kinematical correlation between E_n and θ_{lab} can be seen, which is associated with the ground state or excitation of states at low excitation energies in ^{56}Cu produced in the ^{56}Ni(p,n) reaction (see Fig. 1 for comparison). Figure 4(b) shows the spectrum associated with the detection of ^{55}Ni fragments in the spectrograph. Two broad kinematic correlations can be distinguished, corresponding to the excitation of states in ^{56}Cu near approximately 3 and 12 MeV. Such kinematic correlations are barely visible in Fig. 4(c) (associated with the detection of ^{54}Co in the spectrograph) and completely absent in Fig. 4(d) (associated with the detection of ^{53}Co in the spectrograph).

Fig. 5 shows similar scatter plots but for events associated with the ^{55}Co beam component. Clear kinematic correlations are visible in Figs. 5(a) and (b) owing to the excitation of different levels in ^{55}Ni and associated with the detection of ^{55}Ni and ^{54}Co in the spectrograph, respectively. Such correlations are difficult to distinguish in

TABLE I. Overview of secondary beam components and associated beam residues, reactions, and reaction types.

Beam components	Residue detected in S800	Reaction channel	Reaction type
^{56}Ni	^{56}Cu	^{56}Ni$(p,n)^{56}$Cu	CE reaction
	^{55}Ni	^{56}Ni$(p,n)^{56}$Cu$\rightarrow^{55}$Ni$+p$	CE reaction
		^{56}Ni$+p\rightarrow^{55}$Ni$+p+n$	Knockout/fragmentation reaction
	^{54}Co	^{56}Ni$(p,n)^{56}$Cu $\rightarrow^{54}$Co$+p+p$	CE reaction
		^{56}Ni$+p\rightarrow^{54}$Co$+2p+n$	Knockout/fragmentation reaction
	^{53}Co	^{56}Ni$+p\rightarrow^{53}$Co$+3p+n$	Knockout/fragmentation reaction
^{55}Co	^{55}Ni	^{55}Co$(p,n)^{55}$Ni	CE reaction
	^{54}Co	^{55}Co$(p,n)^{55}$Ni$\rightarrow^{54}$Co$+p$	CE reaction
		^{55}Co$+p\rightarrow^{54}$Co$+p+n$	Knockout/fragmentation reaction
	^{53}Fe	^{55}Co$(p,n)^{55}$Ni $\rightarrow^{53}$Co$+p+p$	CE reaction
		^{55}Co$+p\rightarrow^{53}$Fe$+2p+n$	Knockout/fragmentation reaction
	^{52}Fe	^{55}Co$+p\rightarrow^{52}$Fe$+3p+n$	Knockout/fragmentation reaction

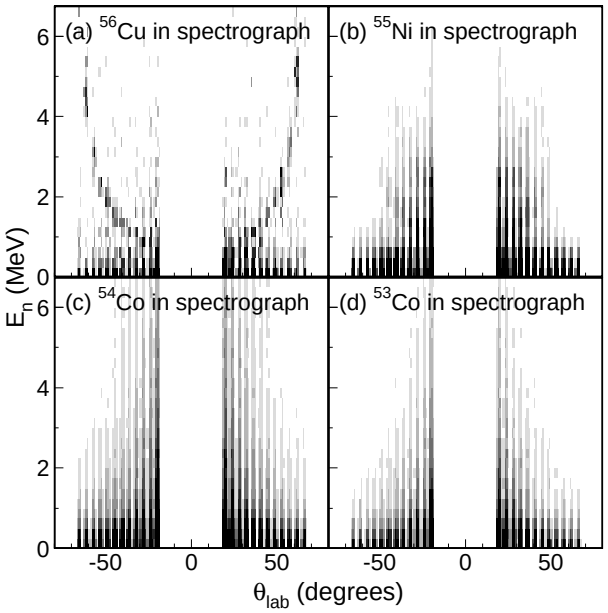

FIG. 4. Neutron spectra as a function of neutron energy (E_n) and laboratory angle (θ_{lab}) for the ^{56}Ni beam component and for events associated with the heavy fragments in the spectrograph: (a) ^{56}Cu, (b) ^{55}Ni, (c) ^{54}Co, and (d) ^{53}Co.

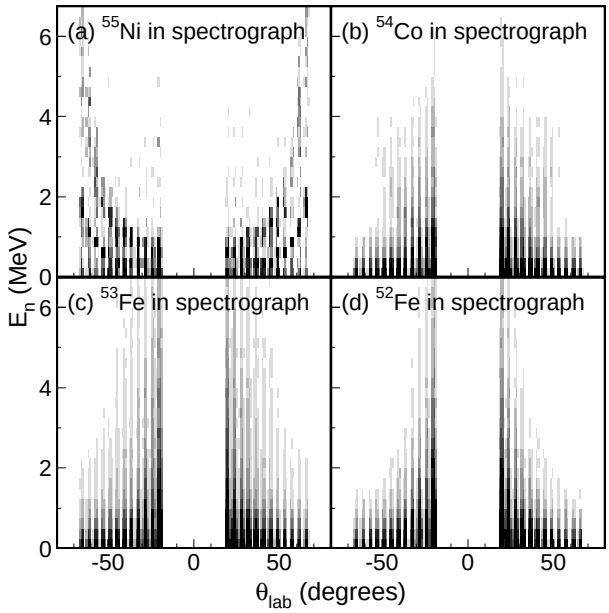

FIG. 5. Same spectra as in Fig. 4, but for the ^{55}Co beam component and for events associated with the heavy fragments: (a) ^{55}Ni, (b) ^{54}Co, (c) ^{53}Fe, and (d) ^{52}Fe.

Figs. 5(c) (^{53}Fe detected in the spectrograph), and completely absent in Figs. 5(d) (^{52}Fe detected in the spectrograph).

Regardless of the reaction channel, two sources of background are present in the scatter plots shown in Figs. 4 and 5. In Figs. 4(d) and 5(d), they are the sole contributors to the two-dimensional spectra. The first source of background, associated with the events evenly distributed in $\theta_{\rm lab}$ for $E_n < 0.5$ MeV, is due to random coincidences, which can be subtracted by using the method described in Sec. II C. The second source, associated with neutrons predominantly observed at forward scattering angles, is due to knockout/fragmentation reactions in which neutrons rescatter from material downstream of the target into the detector array.

B. Corrections for neutron-detection efficiency

The neutron-detection efficiency was estimated as a function of excitation energy (E_x) and center-of-mass scattering angle ($\theta_{\rm c.m.}$) by using a Monte Carlo simulation with the GEANT3 package [38]. For each simulated (p,n)-reaction event, the E_x and $\theta_{\rm c.m.}$ values were reconstructed by taking into account the intrinsic neutron-detection efficiency per bar (see Sec. II C), the geometrical acceptance, and the time resolution of LENDA. The effects of the energy loss of beam particles in the target prior to the reaction were also taken into account. Simulated events were grouped into 2°-wide bins in $\theta_{\rm c.m.}$ (the estimated resolution in the reconstructed $\theta_{\rm c.m.}$ was

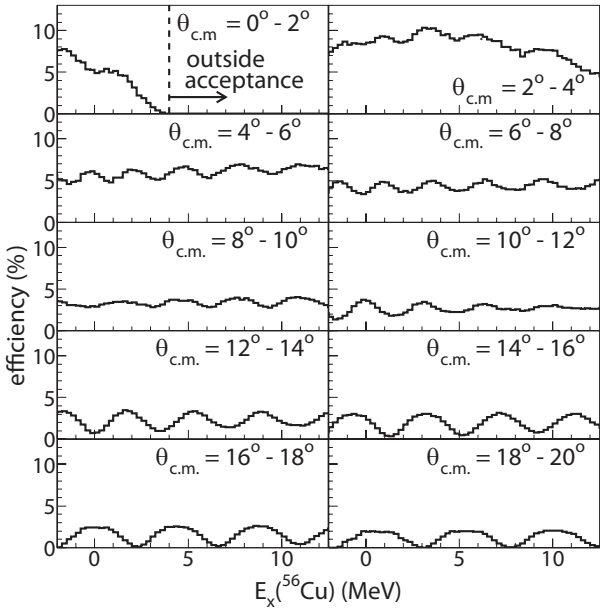

FIG. 6. Simulated overall efficiency of LENDA as function of the excitation energy in ^{56}Cu (E_x) and the scattering angle in the center-of-mass system ($\theta_{c.m.}$), including the intrinsic neutron-detection efficiency plus the geometrical acceptance, for the ^{56}Ni(p,n) reaction. The time resolution of LENDA and the effect of the beam energy loss in the target are also taken into account. See text for the details.

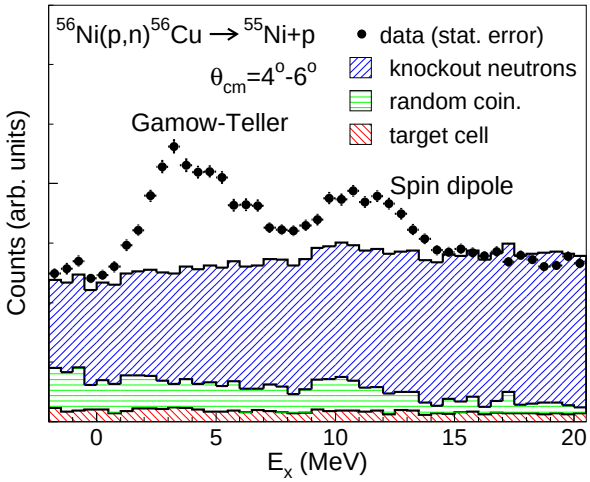

FIG. 7. (Color online) An example of the reconstructed spectrum (filled circles) for the ^{56}Ni$(p,n)^{56}$Cu reaction following the decay by single proton emission from ^{56}Cu. Shaded areas indicate the simulated or measured contributions from the backgrounds due to knockout/fragmentation reactions, random coincidence, and reactions caused by the target cell (see text).

better than 0.5°). The efficiencies for angular bins up to $\theta_{\rm c.m.} = 20°$ are displayed as a function of excitation energy in ^{56}Cu in Fig. 6 for the ^{56}Ni(p,n) reaction. Similar simulations were performed for the efficiency as a function of excitation energy in ^{55}Ni for the ^{55}Co(p,n) reaction.

With increasing values of $\theta_{\rm c.m.}$, periodic structures in the efficiency as a function of excitation energy become apparent. This is because the excitation energy becomes predominantly dependent on the neutron laboratory angle at backward center-of-mass angles (see Fig. 1) and the gaps between the LENDA scintillator bars cause cusps in the efficiency. In the regions where the efficiencies becomes very small, the simulation is strongly dependent on the precise matching of the locations of the bars in the simulation to the real locations during the experiment. To avoid artificial biases due to the uncertainties in the alignment of each bar, events in the region where the efficiency is smaller than 20% of the maximum efficiency, for a given bin in $\theta_{c.m.}$, were excluded from the analysis.

From the experimental data, E_x and $\theta_{c.m.}$ were reconstructed and grouped into the same bins as used for the calculated efficiencies. The efficiency-corrected yield was then calculated by dividing the number of counts in each bin by the corrsponding calculated efficiency. In Fig. 7 an example of the obtained excitation energy spectrum for events associated with the detection of a ^{55}Ni fragment in S800 is shown (at $\theta_{c.m.} = 4° - 6°$). Clearly, background is present in the spectrum. The subtraction of this background is described in the next section.

C. Background subtraction

The shaded areas in Fig. 7 indicate the various background contributions. There are components: originating from knockout/fragmentation reactions, from random coincidences, and from reactions that took place in the target-cell windows. The contribution from reactions on the target-cell windows were determined by performing measurements with an empty target cell. This was the smallest source of background. The background from random coincidences was obtained as described in Sec. II C. This source of background decreased in intensity with increasing excitation energy. The shape of background due to knockout/fragmentation reactions was modeled by fitting the excitation-energy spectra of events associated with the detection of ^{53}Co (^{52}Fe) in the S800 focal plane with second-order polynomials for events associated with the ^{56}Ni (^{55}Co) beam component. The fitted background component was then scaled to match the spectra containing the CE events for unphysical values of E_x (significantly below 0 MeV and above 18 MeV). Uncertainties in the determination of the three background components were propagated in the further analysis.

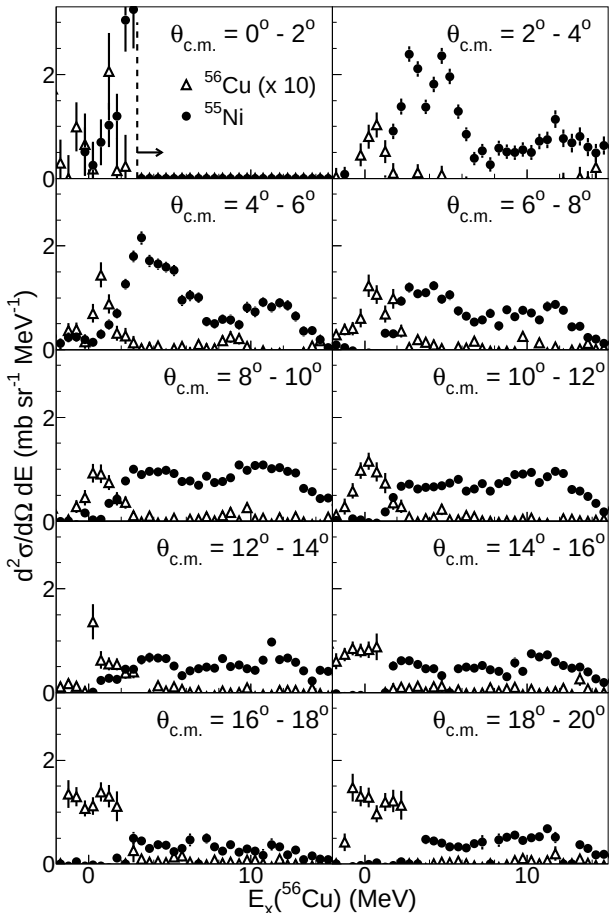

FIG. 8. Double differential cross sections for the ^{56}Ni(p,n) reaction as a function of the excitation-energy (E_x), from 0°–20° with 2° steps. Open triangles and filled circles indicate the components associated with ^{56}Cu and ^{55}Ni, respectively. The cross sections shown with open triangles are magnified by a factor of 10. The E_x regions indicated by arrows are not covered because the corresponding laboratory neutron angles were outside of the acceptance of LENDA.

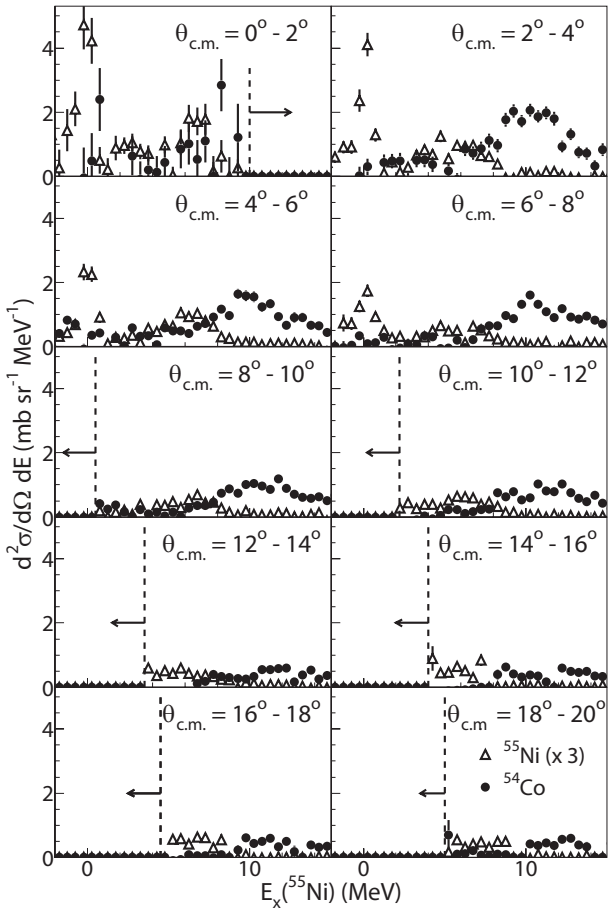

FIG. 9. Same as in Fig. 8, but for the ^{55}Co(p,n) reaction with the components associated with ^{55}Ni and ^{54}Co. The cross sections shown with open triangles are magnified by a factor of 3.

D. Double differential cross sections

Figs. 8 and 9 show the obtained double differential cross sections for the ^{56}Ni$(p,n)^{56}$Cu and ^{55}Co$(p,n)^{55}$Ni reactions, respectively, for each 2°-wide bin. Absolute differential cross sections were determined with an uncertainty of 10% by taking into account the efficiencies of the diamond detector, the S800 focal plane detectors, and the PID gates, the transmission of the beam from the diamond detector to the target and the dead time of the data acquisition system. The upper limit of the excitation-energy region shown in the figures is 15 MeV, sufficiently high to include the main components of the GT strength distribution.

Figure 8 includes two data sets. The first set is associated with the detection of ^{56}Cu in the S800 focal plane. Contributions are primarily restricted to excitation energies below $\sim$ 1 MeV, since the threshold for decay by proton emission in ^{56}Cu ($S_p(^{56}\mathrm{Cu})$), is only 560 keV. Events associated with this channel have differential cross sections that do not strongly vary with scattering angle, indicating that they belong to transitions with angular momentum transfers $\Delta L = 2$ or higher. The second component is associated with the detection of ^{55}Ni in the focal plane of the S800. This channel opens at $S_p(^{56}\mathrm{Cu})$ and dominates the spectra. Differential cross sections in the region between 2 MeV and 8 MeV peak at forward center-of-mass scattering angles, indicative of strong GT ($\Delta L = 0$) transitions. On the other hand, the bump structure around 12 MeV peaks around $\theta_{cm} = 6° - 12°$, indicative of large contributions from spin-dipole (SD) ($\Delta L = 1$) transitions.

In Fig. 9, the data associated with the detection of ^{55}Ni in the S800 focal-plane detectors are shown, i.e. from ^{55}Co(p,n) reactions that populate states in ^{55}Ni below the proton separation energy $S_p(^{55}\mathrm{Ni})$= 4.6 MeV. The spectrum exhibits one sharp peak at 0 MeV, corresponding to the transition to the ground state of ^{55}Ni. Events associated with the detection of ^{55}Ni are observed up to $E_x(^{55}\mathrm{Ni})\approx$ 8 MeV, and peak at forward scattering an-

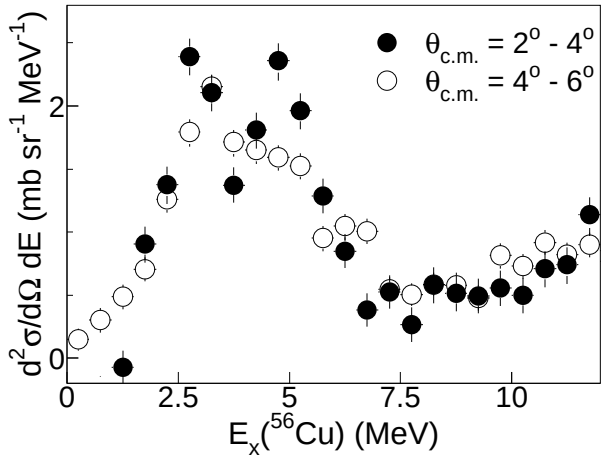

FIG. 10. Comparison of the double differential cross section spectra for the ^{56}Ni(p,n) reaction at $\theta_{\rm c.m.} = 2^\circ - 4^\circ$ (filled markers) and $\theta_{\rm c.m.} = 4^\circ - 6^\circ$ (open markers).

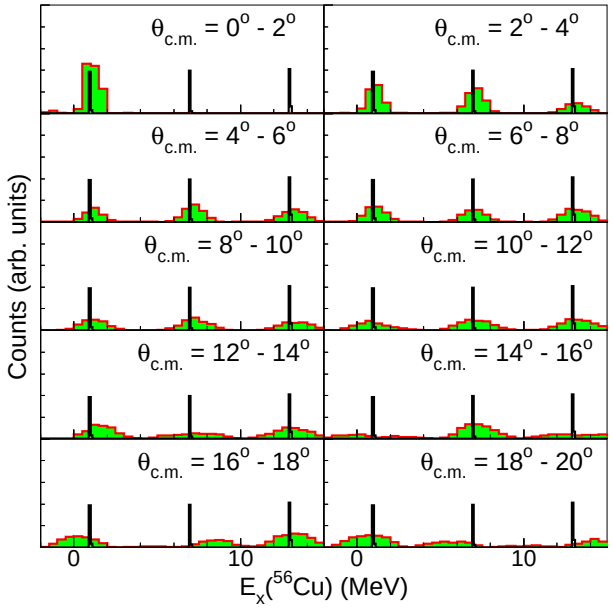

FIG. 11. (Color online) Results of a GEANT3 simulation for the excitation energy resolution for the ^{56}Ni(p,n) reaction as a function of E_x and $\theta_{\rm cm}$, shown with the same binning as in the Fig. 6. The vertical bars are the discrete input excitation energies for the simulation. The response is shown with the shaded areas.

gles, indicative of strong GT contributions to the spectrum. The same is true for events associated with the detection of ^{54}Co in the focal plane of the S800, i.e. after the emission of a proton from ^{55}Ni. A strong, broad bump that peaks at $E_x(^{55}\text{Ni}) \approx 10$ MeV appears to be predominantly due to GT transitions.

The differential cross sections for the branches associated with dual proton emission are not shown in Figs. 8 and 9, because their absolute magnitude could not be established reliably, as explained in Sec. II D. However, the angular distribution of these contributions were examined to confirm that no significant GT strength was present at higher excitation energies.

E. Evaluation of the excitation-energy resolution

Fig. 10 shows the extracted excitation-energy spectra for the ^{56}Ni$(p,n)^{56}$Cu reaction at $\theta_{c.m.} = 2^\circ - 4^\circ$ and $\theta_{\rm c.m.} = 4^\circ - 6^\circ$. The two prominent peaks at $E_x(^{56}\text{Cu})$=3 MeV and 5 MeV at $\theta_{\rm c.m.} = 2^\circ - 4^\circ$ are not well separated at $\theta_{c.m.} = 4^\circ - 6^\circ$ because the resolution in E_x deteriorates with increasing center-of-mass scattering angle. For the purpose of reliably extracting contributions from excitations associated with different transfers of angular momentum on the basis of their angular distributions, the effects of the reduced energy resolution must be taken into account. Therefore, the resolution was evaluated as a function of E_x and $\theta_{\rm c.m.}$ by performing GEANT3 simulations as described above. Discrete values of E_x were input to the simulation, indicated with black bars in Fig. 11. The responses (shaded histograms) are also included in this figure. The resolution in E_x deteriorates rapidly with increasing $\theta_{\rm c.m.}$ and more slowly with increasing E_x and ranges from about 700 keV to 3 MeV (full-width at half-maximum (FWHM))

F. Multipole decomposition analysis

Finally, contributions to the excitation-energy spectra from transitions associated with $\Delta L = 0$ were extracted on the basis of a multipole decomposition analysis (MDA) [39]. The experimental angular distribution for each bin in excitation energy was fitted with a linear combination of calculated angular distributions associated with $\Delta L = 0 - 2$ (The inclusion of additional components with $\Delta L > 2$ did not improve the quality of the fits):

$$\sigma^{\rm calc}(\theta) = \sum_{J^\pi} a_{J^\pi} \sigma^{\rm calc}_{J^\pi}(\theta). \qquad (2)$$

Examples of calculated angular distributions associated with $\Delta L = 0, 1$ and 2 transitions are displayed in Fig. 14. The calculations were performed in Distorted-Wave Impulse Approximation (DWIA) using the computer code DW81 [40] with the effective nucleon-nucleon interaction of Love and Franey at 140 MeV [41]. Optical potentials were taken from Ref. [42] for which the Coulomb component was switched off for the exit channel. One-body transition densities for transitions to final states with different J^π values were calculated in a normal-modes procedure [43] using a harmonic oscillator basis with oscillator parameter $b = 1.970$ fm^{-1}. Single-particle states were filled according to the independent particle model: in ^{56}Ni, neutron and proton orbits were both filled up to the $0f\frac{7}{2}$ shell, while ^{55}Co was assumed to have one proton hole in the $0f\frac{7}{2}$ shell. Final states with

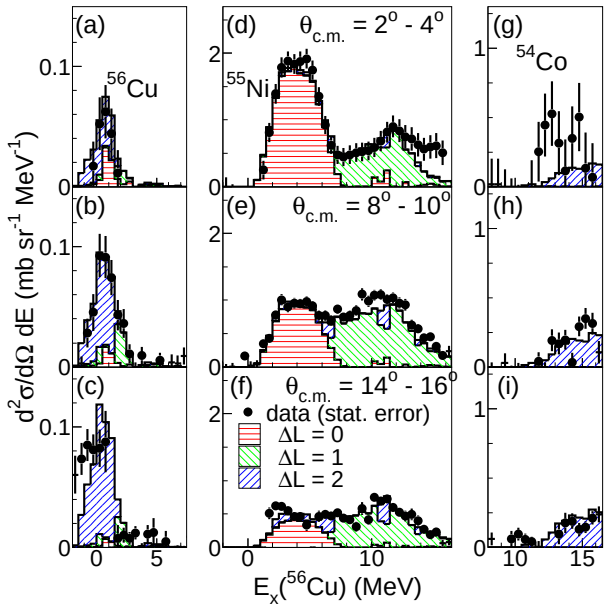

FIG. 12. (Color online) Double differential cross sections (dots) are shown with the MDA results for the ^{56}Ni(p,n) data (shaded areas). Results are presented for $\theta_{c.m.} = 2^\circ - 4^\circ$ (top), $\theta_{c.m.} = 8^\circ - 10^\circ$ (middle), and $\theta_{c.m.} = 14^\circ - 16^\circ$ (bottom) and separately for the decay branches associated with the beam residues of ^{56}Cu (a-c), ^{55}Ni (d-f), and ^{54}Co (g-i). The absolute magnitude of the cross sections with the ^{54}Co beam residue is arbitrary.

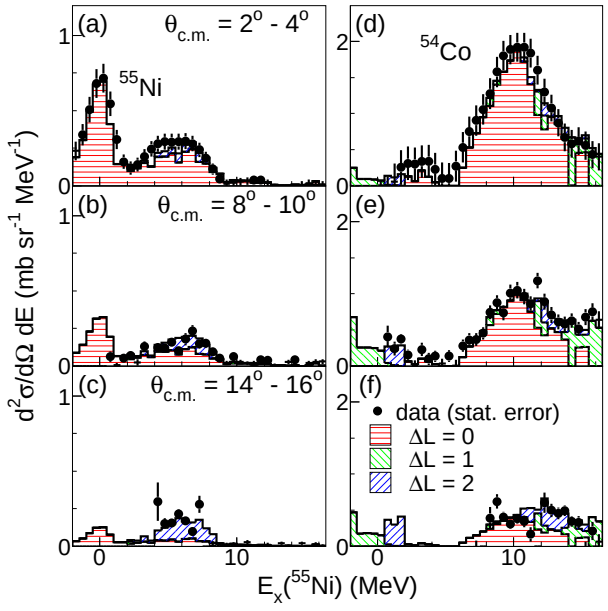

FIG. 13. (Color online) Same as in Fig. 12, but for the ^{55}Co(p,n) data. Results are presented for $\theta_{c.m.} = 2^\circ - 4^\circ$ (top), $\theta_{c.m.} = 8^\circ - 10^\circ$ (middle), and $\theta_{c.m.} = 14^\circ - 16^\circ$ (bottom) and separately for the decay branches with the ^{55}Ni (a-c) and ^{54}Co (d-f) residues. The branch with two-proton emission does not contribute in the energy region of interest below 15 MeV, and is not shown herein.

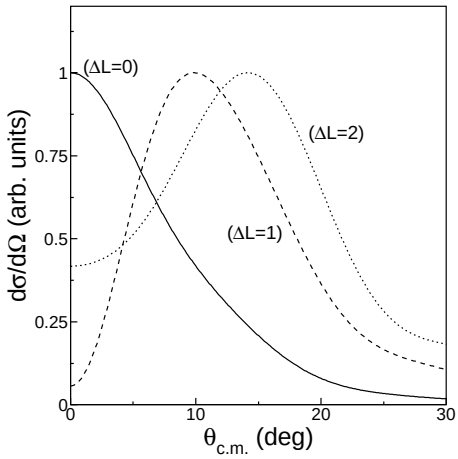

FIG. 14. Angular distribution for transitions with $\Delta L = 0, 1$ and 2 in the ^{56}Ni(p,n) reaction at 110 MeV/u. Details of the calculations are provided in the text.

$J^\pi = 1^+(\Delta L = 0), 1^-, 2^-(\Delta L = 1)$, and $2^+(\Delta L = 2)$ were included. In contrast to our original report in Ref. [10], transitions to 0^- states ($\Delta L = 1$) were excluded because the associated cross sections are expected to be significantly smaller than those associated with transitions to 1^- and 2^- states. This significantly improved the stability and quality of the fitting procedure, thereby reducing the systematic uncertainties. Angular distributions of final states associated with $\Delta L = 2$ ($J^\pi = 1^+, 2^+, 3^+$) were very similar. Hence only the $J^\pi = 2^+$ contribution was included in the fit. To avoid artificial biases due to the deterioration of the excitation energy resolution with increasing center-of-mass angle, the spectra at forward angles were smeared with Gaussian line shapes so that the excitation energy resolution becomes 1.2 MeV at forward angles ($\theta_{cm} < 8^\circ$), independent of excitation energy and scattering angle.

In Fig. 12, the results of the MDA for the ^{56}Ni(p,n) reaction are shown for three scattering angles, and separately for events associated with the detection of ^{56}Cu, ^{55}Ni, and ^{54}Co in the spectrograph. The results for the ^{55}Co(p,n)^{55}Ni reaction are shown in Fig. 13, separately for the detection of ^{55}Ni and ^{54}Co in the spectrograph.

The ^{56}Ni(p,n) spectrum is dominated by GT transitions up to E_x(^{56}Cu)=8 MeV, except at the lowest excitation energies (associated with the detection of ^{56}Cu in the S800), where quadrupole transitions are dominant. Between 8 MeV and 14 MeV, dipole transitions are dominant. At the highest excitation energies, quadrupole transitions become dominant. Similarly, the ^{55}Co(p,n) spectrum is dominated by GT transitions up to 15 MeV, with minor contributions from dipole and quadrupole excitations in the region above 10 MeV and 4 MeV, respectively. For both reactions, no significant GT contributions to the spectra were uncovered at excitation energies above 15 MeV, i.e. associated with branches for decay by two-proton emission.

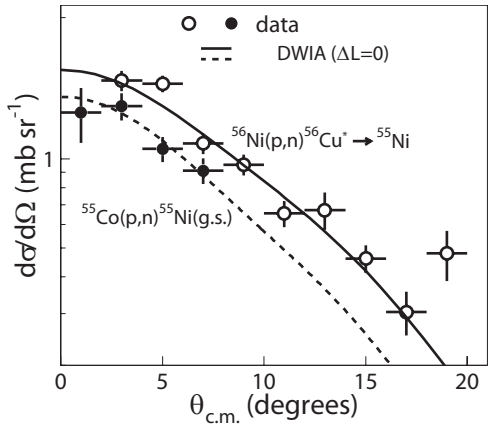

FIG. 15. Differential cross sections for the ^{55}Co($\frac{7}{2}^-$,g.s.)$(p,n)^{55}$Ni($\frac{7}{2}^-$,g.s.) reaction and the ^{56}Ni$(p,n)^{56}$Cu reaction at $E_x(^{56}\mathrm{Cu})$=4–4.5 MeV (right). The angular range for the former transition is limited to $\theta_{c.m.} < 10^\circ$ by the acceptance of LENDA. In both cases the angular distribution fits well with a GT ($\Delta L = 0$) angular distribution calculated with in DWIA. The 0° differential cross section for the ^{55}Co($\frac{7}{2}^-$,g.s.)$(p,n)^{55}$Ni($\frac{7}{2}^-$,g.s.) reaction is derived by extrapolating the data points to 0° using the fitted angular distribution.

G. Gamow-Teller unit cross section $\hat{\sigma}_{\mathrm{GT}}$

GT strengths were derived from the cross sections associated with $\Delta L = 0$ excitations extracted in the MDA on the basis of Eq. (1). The GT unit cross section $\hat{\sigma}_{\mathrm{GT}}$ was determined by using the ^{55}Co($\frac{7}{2}^-$,g.s.)$(p,n)^{55}$Ni($\frac{7}{2}^-$,g.s.) reaction, which can clearly be observed in Fig. 13(a). Due to the angular coverage of LENDA in the present experiment, differential cross sections for this transition could only be extracted for $\theta_{\mathrm{c.m.}} < 8^\circ$ and are shown in Fig. 15 (filled markers). The 0° differential cross section, $\sigma_{\Delta L=0}(0^\circ)$, was determined to be 1.62±0.09 mb/sr by fitting differential cross sections calculated in DWIA (also shown in Fig. 15) to the experimental angular distribution. Since the ground state of ^{55}Ni is the isobaric analog of the ground state of ^{55}Co, $\sigma_{\Delta L=0}(0^\circ)$ for this transition has both GT and Fermi ($\Delta L = 0, \Delta S = 0$) contributions: $\sigma_{\Delta L=0}(0^\circ) = \sigma_{GT}(0^\circ) + \sigma_F(0^\circ)$. The fraction due to the GT component, defined as $f_{GT} = \sigma_{GT}(0^\circ)/\sigma_{\Delta L=0}(0^\circ)$, was reliably estimated (0.51 ± 0.03) by using the known Fermi ($B(\mathrm{F}) = N - Z = 1$; assuming full exhaustion of the Fermi sum rule) and GT ($B(\mathrm{GT}) = 0.267$ [30]) strengths for this transition, as well as the ratio $R^2 = \frac{\hat{\sigma}_{\mathrm{GT}}}{\hat{\sigma}_{\mathrm{F}}} = 4.0 \pm 0.2$. $\hat{\sigma}_{\mathrm{F}}$ is the unit cross section for Fermi transitions, similar to that for GT transitions expressed in Eq. (1). The R^2 value was calculated from its well-established dependence on beam energy [29]. The values of $F(q,\omega)$ for the Fermi and GT contributions were determined in DWIA and differed by less than 1%. We found that $\hat{\sigma}_{\mathrm{GT}} = 3.2 \pm 0.5$ mb/sr, which is consistent with the value of 3.5 ± 0.2 reported for the ^{58}Ni(p,n) reaction at 120 MeV [29].

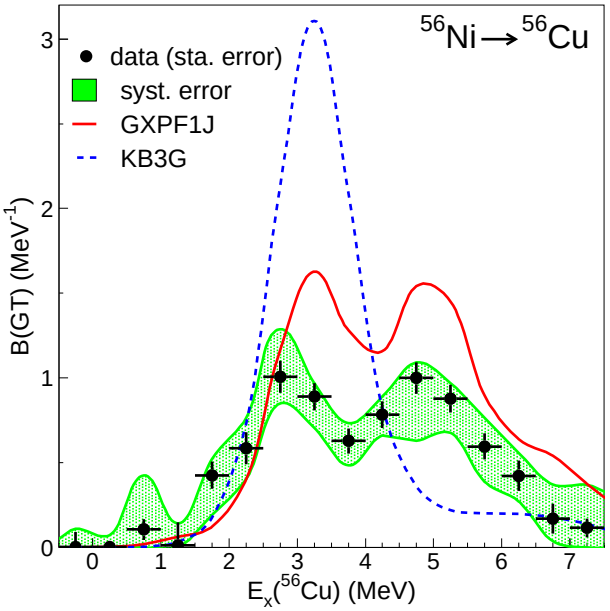

FIG. 16. (Color online) Extracted strength distribution for GT transitions from ^{56}Ni to ^{56}Cu (dots) and the comparison with shell-model calculations using the KB3G and GXPF1J interactions (continuous and dashed curves). The shaded bands indicate the systematic uncertainties mainly due to the subtraction of neutron-knockout/fragmentation background. The uncertainty in the unit cross section is not included in the band. See the text for the details of the systematic uncertainties.

H. Gamow-Teller strengths

Given the GT unit cross section derived from the ^{55}Co data, and by calculating $F(q,\omega)$ in Eq. (1) in DWIA as a function of excitation energy, the GT strengths for the ^{56}Ni$(p,n)^{56}$Cu and ^{55}Co$(p,n)^{55}$Ni reactions could be extracted for all relevant excitation energies from the values of $\sigma_{\Delta L=0}$ extracted in the MDA. The GT strengths associated with different beam fragments were then combined in a single strength distribution as shown in Figs. 16 and 17. In the case of ^{56}Ni(p,n) reaction, nearly all the yield (> 95%) for $1 < E_x(^{56}\mathrm{Cu}) < 8$ MeV was due to GT transitions. Consequently, the unsmeared distribution shown with filled markers in Fig. 10 was used in the description of the final GT strength distribution shown in Fig. 16.

The boundaries of the shaded bands in Fig. 16 and 17 indicate the upper and lower limits of the systematic uncertainties in the extracted GT strengths. The largest source (< 20%, depending on excitation energy) of systematic uncertainty came from the background subtraction due to neutrons detected in LENDA from knock-out/fragmentation reactions (see Fig. 7). It was estimated by changing the fitting functions used for modeling this source of background (e.g. a linear function instead of a second-order polynomial). The effects of changing the PID gates (see Section II D) (either making them wider or narrower) were also included in this error

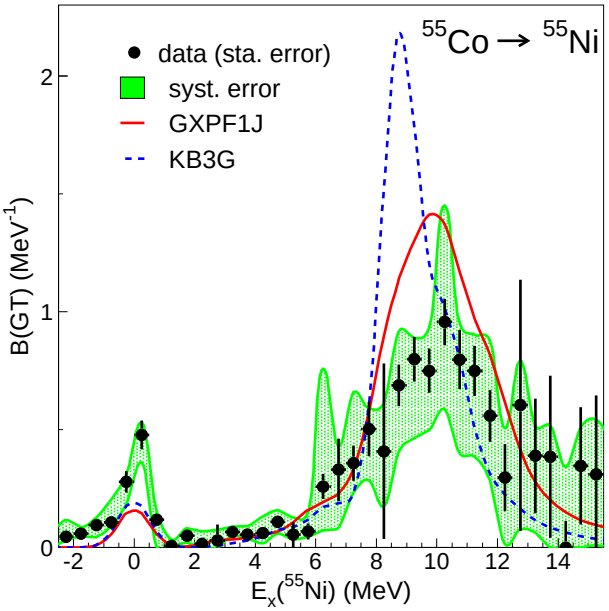

FIG. 17. (Color online) Same as Fig. 16, but for GT transitions from ^{55}Co to ^{55}Ni (dots) and with their shell-model calculations using the KB3G and GXPF1J interactions (continuous and dashed curves).

analysis.

The second major source of systematic uncertainty comes from the characterization of LENDA ($< 15\%$, depending on excitation energy). To evaluate this uncertainty, different thresholds for the detection of neutrons were chosen (in software) simultaneously in the efficiency calculations and in the analysis of the data. The effects of excluding double-hit events (e.g., due to cross-talk between neighboring bars), and uncertainties in various input parameters for the Monte-Carlo simulations (e.g. target thickness, beam profile at the target, location of the bars) were also included in the estimation of this source of background.

Additional sources of systematic uncertainties were related to the inputs for the DWIA calculations used in the MDA ($< 5\%$), which were estimated by varying the input parameters within reasonable boundaries, and the effects of smearing the excitation-energy spectra (see Section III E) ($\sim 2\%$) for the purpose of the MDA analysis.

Since the different sources of systematic errors are not independent, the overall systematic uncertainty was estimated by re-performing the full analysis many times with different inputs/choices for the parameters affecting these individual sources of uncertainty. On the basis of that procedure, we found that the combinatorial effect of all systematic uncertainties was $\sim 30\%$. The overall uncertainty in the estimation of $\hat{\sigma}_{\rm GT}$ (15%, see Section III G) is not included in this overall uncertainty, as it simply scales all extracted GT strengths up or down.

IV. COMPARISON WITH SHELL-MODEL CALCULATIONS

The GT strength distribution extracted from the ^{56}Ni(p,n) reaction shown in Fig. 16 was compared with shell-model calculations performed in the full pf shell by employing the KB3G [23] and GXPF1J [26] interactions. The theoretical strength distributions, also shown in Fig. 16, have been smeared by the experimental excitation-energy resolution and scaled by a quenching factor of $(0.74)^2$ [44] to account for degrees of freedom not included in the shell-model calculations. Please note that in Ref. [10] the GXPF1A interaction was used instead of the GXPF1J interaction. GXPF1A was made by improving GXPF1 [25] by taking into account additional new experimental data of neutron-rich Ca, Ti and Cr isotopes with $N >32$. It was further modified to reproduce the peak position of the M1 strength in ^{48}Ca at 10.23 MeV (see Ref. [27] for more details). GXPF1A predicts that peak position to be at 10.90 MeV. Therefore, the GXPF1J interaction is considered to be more suitable for the calculation of spin-isospin modes in pf-shell nuclei, although in the calculation of GT strengths from ^{56}Ni and ^{55}Co the differences between the calculations with the GXPF1A and GXPF1J interaction are minor.

The shell-model calculations with the GXPF1J interaction produce a GT strength distribution in ^{56}Cu that is shifted up in excitation energy by about 0.5 MeV relative to the strength distribution extracted from the data. On the other hand, the calculation with the KB3G interaction exhibits a strong peak at an excitation energy just above 3 MeV, and much less strength at higher energies, in clear contrast to the experimental results.

In both sets of shell-model calculations, the GT strength is dominated by contributions from $f_{7/2}$–$f_{5/2}$ $1p-1h$ excitations. However, due to weaker spin-orbit and residual proton-neutron potentials in the case of the KB3G interaction, the average excitation energy for the GT transitions is lower by about 1.5 MeV compared to the GXPF1J interaction. Since the level density rapidly increases with increasing excitation energy, the spreading of the strength is enhanced in the shell-model calculation with the GXPF1J interaction, which results in a broadening and fragmentation of the strength distribution. The effect is enhanced by the fact that the level-density for 1^+ states in ^{56}Cu in the calculation with the GXPF1J interaction below an excitation energy of 8 MeV is about double of that level density in the calculation with the KB3G interaction.

A similar effect is observed for the GT strength distribution in ^{55}Ni, as shown in Fig. 17. The GT strengths from the shell-model calculations with the GXPF1J interaction match the distribution extracted from the ^{55}Co(p,n) data quite well. The calculation employing the KB3G interaction puts the GT strength on average at lower excitation energies and is more concentrated. Note that although the two shell-model calculations do equally

TABLE II. Comparison of the integrated GT strengths between experimental data and theoretical predictions.

	E_x (MeV)	Data[a]	GXPF1J(KB3G)[b]
^{56}Ni→^{56}Cu	0 – 7	3.8 ± 0.2(stat.)$\pm$0.8(syst.)	5.5 (5.2)
^{55}Co→^{55}Ni(g.s.)	0	0.267 (from Ref. [30])	0.209 (0.253)
^{55}Co→^{55}Ni	0 – 15	5.3 ± 0.5(stat.)$^{+2.5}_{-1.5}$(syst.)	6.8 (6.2)

[a] The quoted error margins do not include the uncertainty in the value for the unit cross section (15%), which would change all strengths by a common scaling factor.
[b] A quenching factor of $(0.74)^2$ [44] has been applied to the shell-model summed strengths.

well (see Table II) in reproducing the GT strength associated with the ground-state to ground-state transition from β-decay (B(GT) = 0.267 [30]), the experimental signal for this transition in Fig. 17 is higher due to the additional contribution from the Fermi component.

Table II shows the comparison of the integrated GT strengths between the experimental values and the theoretical predictions. For both the ^{56}Ni$(p,n)^{56}$Cu and ^{55}Co$(p,n)^{55}$Ni reactions, the GT strengths predicted appear to be slightly higher than those extracted from the data. However, the experimental error margins are significant and there exists an additional uncertainty of 15% due to the determination of $\hat{\sigma}_{\rm GT}$, which scales all GT strength in this work by a common factor. Therefore, it is not clear that the differences between the magnitudes of the summed strengths from the experiment and the theoretical models are significant.

As mentioned above, shell-model calculations using interactions from the "KB family" form the basis of the weak-rate library for astrophysical simulation of Ref. [24]. Since the shell-model calculations with the GXPF1J interaction provide a better match to the experimental GT distribution from ^{56}Ni, it can be concluded that the existing weak-rate library can be further improved. The possible improvements are difficult to quantify, but based on a study of a limited number of nuclei in the pf-shell [4], gains in precision of up to about 30% appear feasible for stellar densities in excess of 10^7 g/cm^3. The present results provide key information to achieve such improvements.

V. CONCLUSION

In summary, a new method to study (p,n) charge-exchange experiments at intermediate energies in inverse kinematics is described on the basis of an experiment aimed at extracting Gamow-Teller strength distributions from ^{55}Co and ^{56}Ni. As part of the experiment, the Low-Energy Neutron Detector Array (LENDA) and a new liquid fydrogen target were commissioned. The new method for performing (p,n) experiments in inverse kinematics is attractive as it can be used for studying isovector transitions in a wide variety of rare isotopes up to high excitation energies. The excitation energy and center-of-mass scattering angle can be extracted, allowing for analysis of the data much like for charge-exchange experiments with stable isotopes in forward kinematics. Although the experiments presented in this paper were primarily motivated by the need to provide data to improve the estimates for weak-reaction rates of relevance for astrophysics, the method opens the door for experiments aimed at other topics as well, such as the study of isovector giant resonances in rare isotopes. Certain improvements to the method are likely possible; in particular, it would be desirable to reduce the amount of background due to neutrons produced in contaminant reactions. Although it was possible to subtract contributions from such sources of background, it introduced significant systematical uncertainties.

The extracted GT strength distributions from the ^{55}Co(p,n) and ^{56}Ni(p,n) reactions were compared with shell-model calculations that use the GXPF1J and KB3G interactions in the full pf shell-model space. It was found that calculations with the KB3G interaction produce strength distributions that are more concentrated and peak at excitation energies significantly lower than seen in the data. The calculations with the GXPF1J interaction matched the experimental GT strength distributions much better. It is concluded that weak-reaction rate tables compiled for nuclei in the pf-shell by using shell-model calculations with interactions of the "KB family" can be further improved.

ACKNOWLEDGMENTS

We thank the staff at NSCL for their efforts and support. This work was supported by the US NSF (PHY-0822648 (JINA), PHY-0606007, PHY-0758099 and PHY-1068217), the US DOE (DE-FG02-94ER40848) and the Research Corporation for Science Advancement.

[1] F. Osterfeld, Rev. Mod. Phys. **64**, 491 (1992).
[2] M. N. Harakeh and A. van der Woude, *Giant Resonances: Fundamental High-Frequency Modes of Nuclear Excitations* (Oxford University Press, New York, 2001).

[3] K. Langanke and G. Martínez-Pinedo, Rev. Mod. Phys. **75**, 819 (2003), and references therein.
[4] A. L. Cole, T. S. Anderson, R. G. T. Zegers, Sam M. Austin, B. A. Brown, L. Valdez, S. Gupta, G. W. Hitt, and O. Fawwaz, arXiv:1204.1994[nucl-ex] (2012), and to be published.
[5] J. A. Brown *et al.*, Phys. Rev. C **54**, R2105 (1996).
[6] T. Nakamura *et al.*, Phys. Lett. **B493**, 209 (2000).
[7] R. G. T. Zegers *et al.*, Phys. Rev. Lett. **104**, 212504 (2010).
[8] Y. Satou *et al.*, Phys. Lett. **B697**, 459 (2011).
[9] R. Meharchand *et al.*, Phys. Rev. Lett. **108**, 122501 (2012).
[10] M. Sasano *et al.*, Phys. Rev. Lett. **107**, 202501 (2011).
[11] A. Heger, K. Langanke, G. Martínez-Pinedo, and S. E. Woosley, Phys. Rev. Lett. **86**, 1678 (2001).
[12] A. Heger, S. E. Woosley, G. Martínez-Pinedo, and K. Langanke, Astro Phys. J. **560**, 307 (2001).
[13] W. R. Hix *et al.*, Phys. Rev. Lett **91**, 201102 (2003).
[14] F. Brachwitz *et al.*, Astrophys. J. **536**, 934 (2000).
[15] K. Iwamoto *et al.*, Ap. J. Supp. Ser. **125**, 439 (1999).
[16] K. L. Yurkewicz *et al.*, Phys. Rev. **C70**, 054319 (2004).
[17] K. L. Yurkewicz *et al.*, Phys. Rev. **C74**, 024304 (2006).
[18] J. S. Berryman *et al.*, Phys. Rev. **C79**, 064305 (2009).
[19] K. Minamisono *et al.*, Phys. Rev. Lett. **96**, 102501 (2006).
[20] J. Lee, M. B. Tsang, W. G. Lynch, M. Horoi, and S. C. Su, Phys. Rev. **C79**, 054611 (2009).
[21] A. F. Lisetskiy *et al.*, Phys. Rev. C **68**, 034316 (2003).
[22] E. Caurier, F. Nowacki, A. Poves, and J. Retamosa, Nucl. Phys. A **654**, 973c (1999).
[23] A. Poves, J. Sánchez-Solano, E. Caurier, and F. Nowacki, Nucl. Phys. **A694**, 157 (2001).
[24] K. Langanke and G. Martínez-Pinedo, At. Data and Nucl. Data Tables **79**, 146 (2001).
[25] M. Honma, T. Otsuka, B. A. Brown, and T. Mizusaki, Phys. Rev. C **69**, 034335 (2004).
[26] M. Honma *et al.*, J. Phys. Conf. Series **20**, 7 (2005).
[27] T. Suzuki, M. Honma, H. Mao, T. Otsuka, and T. Kajino, Phys. Rev. C **83**, 044619 (2011).
[28] N. Anantaraman *et al.*, Phys. Rev. C **78**, 065803 (2008).
[29] T. N. Taddeucci *et al.*, Nucl. Phys. **A469**, 125 (1987).
[30] J. Äystö *et al.*, Phys. Lett. **B138**, 369 (1984).
[31] D. Morrissey *et al.*, Nucl. Instrum. Meth. Phys. Res. B **204**, 90 (2003).
[32] A. Stolz, M. Behravan, M. Regmi, and B. Golding, Diam. Relat. Mater. **15**, 807 (2006).
[33] D. Bazin *et al.*, Nucl. Instrum. Meth. Phys. Res. B **204**, 629 (2003).
[34] G. Perdikakis *et al.*, Nucl. Instrum. Meth. Phys. Res. A **686**, 117 (2012).
[35] G. Perdikakis *et al.*, Phys. Rev. C **83**, 054614 (2011).
[36] Monte Carlo NParticle Transport Code System, MCNP5-1.60 and MCNPX-2.7.0, http://www-rsicc.ornl.gov/codes/ccc/ccc7/ccc-740.html.
[37] J. Yurkon, D. Bazin, W. Benenson, D. J. Morrissey, B. M. Sherrill, D. Swan, and R. Swanson, Nucl. Instrum. Meth. Phys. Res. A **422**, 291 (1999).
[38] Http://wwwasd.web.cern.ch/wwwasd/geant/.
[39] T. Wakasa *et al.*, Phys. Rev. C **55**, 2909 (1997).
[40] Program DWBA70, R. Schaeffer and J. Raynal (Unpublished); Extended Version DW81 by J. R. Comfort (Unpublished).
[41] M. A. Franey and W. G. Love, Phys. Rev. C **31**, 488 (1985).
[42] A. Nadasen *et al.*, Phys. Rev. C **23**, 1023 (1981).
[43] M. A. Hofstee *et al.*, Nucl. Phys. A **588**, 729 (1995).
[44] G. Martínez-Pinedo, A. Poves, E. Caurier, and A. P. Zuker, Phys. Rev. C **53**, R2602 (1996).